PHYSICAL REVIEW B **86**, 195133 (2012)

Structure and physical properties of the layered iron oxychalcogenide $BaFe_2Se_2O$

Hechang Lei(雷和畅),[1] Hyejin Ryu(류혜진),[1,2] V. Ivanovski,[3] J. B. Warren,[4] A. I. Frenkel,[5] B. Cekic,[3] Wei-Guo Yin(尹卫国),[1] and C. Petrovic[1,2]

[1]*Condensed Matter Physics and Materials Science Department, Brookhaven National Laboratory, Upton, New York 11973, USA*

[2]*Department of Physics and Astronomy, Stony Brook University, Stony Brook, New York 11794-3800, USA*

[3]*Institute of Nuclear Sciences Vinca, University of Belgrade, Belgrade 11001, Serbia*

[4]*Instrumentation Division, Brookhaven National Laboratory, Upton, New York 11973, USA*

[5]*Physics Department, Yeshiva University, 245 Lexington Avenue, New York, New York 10016, USA*

(Received 28 June 2012; published 26 November 2012)

We have successfully synthesized a layered iron oxychalcogenide $BaFe_2Se_2O$ single crystal. This compound is built up of Ba and Fe-Se(O) layers alternatively stacked along the *c* axis. The Fe-Se(O) layers contain double chains of edge-shared Fe-Se(O) tetrahedra that propagate along the *b* axis and are bridged by oxygen along the *a* axis. Physical property measurements indicate that $BaFe_2Se_2O$ is a semiconductor without the Curie-Weiss behavior up to 350 K. There is a possible long-range antiferromagnetic transition at 240 K, corresponding to the peak in specific-heat measurement, and two transitions at 115 K and 43 K where magnetic susceptibility drops abruptly. The magnetic entropy up to 300 K is much smaller than the expected value for Fe^{2+} in tetrahedral crystal fields and the Mössbauer spectrum indicates that long-range magnetic order is unlikely at 294 K. Our results suggest that $BaFe_2Se_2O$ is a magnetic insulator at the borderline between a long-range antiferromagnetic spin ordering and possible spin dimerization.

DOI: 10.1103/PhysRevB.86.195133 PACS number(s): 75.50.Ee, 75.10.Pq, 75.30.Gw, 75.47.Np

I. INTRODUCTION

The discovery of layered iron oxypnictide [*Ln*(O,F)FeAs; *Ln* = rare-earth elements, 1111 type] superconductors with T_c up to 56 K[1] has stimulated great interest in mixed-anion materials. Mixed anions from the same row of the Mendeleev periodic table tend to randomly occupy the same crystallographic site (anion disorder) because of the relatively similar sizes. On the other hand, if the anions are from different rows (oxysulfide or oxyselenide compounds, for example), the distinctive difference of anion sizes and ionic polarization might lead to ordered occupancy in the different crystallographic sites (anion order), often forming layered crystal structure.[2]

The mixed-anion compounds have attracted some interest during the exploration of novel cuprate high-temperature superconductors. Halooxocuprates are example where copper ions are coordinated with four oxygen ions, forming the CuO_2 sheet, whereas the halogen ion usually occupies a so-called apical site.[3] With proper electron or hole doping, halooxocuprates will become superconductors.[3] Besides superconductivity, mixed-anion materials also exhibit diverse physical properties. Copper oxychalcogenides *Ln*CuO*Ch* (*Ch* = S, Se, and Te), isostructural to 1111-type iron-based superconductors, are wide-gap *p*-type semiconductors with transparent *p*-type conductivity, photoluminescence, and large third-order optical nonlinearity.[4–6] Transition-metal oxychalcogenides $Ln_2O_2TM_2OCh_2$ (*TM* = Mn, Fe, and Co) contain layers built up by the edge-shared octahedral unit $[TM_2OCh_2]^{2-}$. These materials show strong electron-electron interactions (Mott insulators) on the two-dimensional (2D) frustrated antiferromagnetic (AFM) checkerboard spin lattice.[7–9]

The materials with $[TM_2OCh_2]^{2-}$ layers exhibit similar structural diversity to iron-based superconductors. This is understandable since new compounds can be obtained by simply replacing $[FeAs]^-$ layers with $[TM_2OCh_2]^{2-}$ layers, such as *Ln*OFeAs $\rightarrow$ $Ln_2O_2TM_2OCh_2$, *AE*FFeAs (*AE* = alkali-earth metals) $\rightarrow$ $AE_2F_2TM_2OCh_2$,[10–13] and *A*FeAs (*A* = alkali metals) $\rightarrow$ $Na_2Fe_2OSe_2$.[14–16] Thus, it is of considerable interest to explore the structural derivatives of $AEFe_2As_2$ among the oxychalcogenide compounds.

Here, we report the detailed synthesis and physical properties of a layered iron oxychalcogenide $BaFe_2Se_2O$ single crystal. Even though it has the same chemical formula and $[TM_2OCh_2]^{2-}$ layers, the structure is different from other iron oxychalcogenides with similar layers. To the best of our knowledge, $BaFe_2Se_2O$ is the first layered iron oxychalcogenide with an alkali-earth metal. To characterize the material, we performed a number of measurements including x-ray diffraction, x-ray absorption, energy-dispersive x-ray spectroscopy, Mössbauer spectrum, electrical transport, heat capacity, and magnetization. Our results suggest that $BaFe_2Se_2O$ is a magnetic insulator at the borderline between a long-range antiferromagnetic spin ordering and possible spin dimerization.

II. EXPERIMENT

Single crystals of $BaFe_2Se_2O$ were synthesized by a self-flux method. Ba rod, Fe powder, Fe_2O_3 powder, and Se shot were used as starting materials. BaSe was prereacted by reacting a Ba piece with Se shot at 800 °C for 12 hours. BaSe was mixed with other reagents and intimately ground together using an agate pestle and mortar. The ground powder was pressed into pellets, loaded in an alumina crucible, and then sealed in quartz tubes with Ar under the pressure of 0.2 atmospheres. The quartz tubes were heated up to 600 °C in 10 h, kept at 600 °C for 12 h, ramped again to 1100 °C in 12 h, kept at 1100 °C for 12 h, and then cooled slowly at a rate of 3 °C/h to 800 °C; finally the furnace was shut down and the sample was cooled down to room temperature naturally. Black platelike crystals with typical size $2 \times 2 \times 0.5$ mm^3 can

TABLE I. Crystallographic data for $BaFe_2Se_2O$ measured at room temperature.

Chemical formula	$BaFe_2Se_2O$
Formula mass (g/mol)	422.94
Crystal system	orthorhombic
Space group	*Pmmn* (No. 59)
a (nm)	0.98518(7)
b (nm)	0.41332(3)
c (nm)	0.67188(4)
V (nm^3)	0.27359(3)
Z	2
Density (g/cm^3)	5.134
$R1/wR2$ ($F_0 > 4\sigma F_0$)/$R1$ (all data)[a]	0.0459/0.1423/0.0476
Goodness of fit	1.187

[a] $R1 = \Sigma||F_0| - |F_c||/\Sigma|F_0|$, $wR2 = [\Sigma(|F_0^2 - |F_c^2|)^2/\Sigma(wF_0^2)^2]^{1/2}$.

be grown. Except for heat treatment, sample preparation was performed in glove boxes filled with argon.

The crystal structure of $BaFe_2Se_2O$ crystal was identified by single crystal x-ray diffraction (XRD). The data were collected using the Bruker APEX2 software package[17] on a Bruker SMART APEX II single-crystal x-ray diffractometer with graphite-monochromated Mo K_α radiation ($\lambda = 0.071073$ nm) at room temperature. Data processing and an empirical absorption correction were also applied using the APEX2 software package. The structures were solved (direct methods) and refined by full-matrix least-squares procedures on $|F^2|$ using the Bruker SHELXTL program software.[18] The obtained lattice parameters of $BaFe_2Se_2O$ are given in Table I. Atomic coordinates, isotropic displacement parameters, and selected interatomic bond distances and angles are listed in Table II. Phase identity and purity were confirmed by powder x-ray diffraction carried out on a Rigaku miniflex x-ray machine with Cu K_α radiation ($\lambda = 0.15418$ nm). Structural refinements of the powder $BaFe_2Se_2O$ sample was carried out by using RIETICA software.[19]

The average stoichiometry was determined by examination of multiple points using energy-dispersive x-ray spectroscopy (EDX) in a JEOL JSM-6500 scanning electron microscope. The presence of oxygen was confirmed for $BaFe_2Se_2O$, but the exact amount could not be quantified because of experimental limitations. The average atomic ratios determined from EDX are Ba:Fe:Se = 1.00(7):2.2(2):2.0(2), close to the ratio of stoichiometric $BaFe_2Se_2O$.

The Mössbauer spectrum was taken in transmission mode with a $^{57}Co(Rh)$ source at 294 K and the parameters were obtained using WinNormos software.[21] Calibration of the spectrum was performed by laser, and isomer shifts were given with respect to α-Fe.

The x-ray absorption spectra of the Fe and Se K edges were taken in transmission mode on powder samples of $BaFe_2Se_2O$ at the X19A beamline of the National Synchrotron Light Source. Standard procedure was used to extract the extended x-ray absorption fine-structure (EXAFS) from the absorption spectrum.[20] Electrical-transport, heat-capacity, and magnetization measurements were carried out in Quantum Design PPMS-9 and MPMS-XL5.

III. RESULTS AND DISCUSSION

Similar to $K_xFe_{2-y}Se_2$ and $BaFe_2Se_3$,[22,23] the structure of $BaFe_2Se_2O$ is built up by stacking the Ba cations and Fe-Se(O) layers alternatively along the c axis [Fig. 1(a)]. However, within the Fe-Se(O) layers, the connection of Fe-Se(O) tetrahedra in $BaFe_2Se_2O$ is different from those in $K_xFe_{2-y}Se_2$ and $BaFe_2Se_3$. In $BaFe_2Se_2O$, double chains of edge-shared Fe-Se(O) tetrahedra propagate along the Se atoms parallel to the b axis. The Fe-Se(O) double chains are bridged by oxygen along the a axis [Fig. 1(a)]. The bond distances of Fe-Se (~0.25 nm) and Fe-O (~0.19 nm) are very similar to distances in compounds where Fe is also in tetrahedral coordination ($BaFe_2Se_3$: d_{Fe-Se}~ 0.24 nm, Fe_3O_4: d_{Fe-O} ~ 0.19 nm). Because of different bond distances between Fe-Se and Fe-O, Fe atoms are located at the highly distorted tetrahedral environment when compared to other materials with pure Fe-Se tetrahedra. This distortion is also reflected in the significant deviation of bond angles from the value for the ideal tetrahedron (109.5°). The bond angles range up to 130.38(10)° in $BaFe_2Se_2O$, much larger than the values in $BaFe_2Se_3$ and $K_xFe_{2-y}Se_2$.[23,24] Moreover, the different connection of Fe-Se(O) leads to the larger nearest-neighbor Fe-Fe distances [d_{Fe-Fe} (~0.313 nm)] when compared to $BaFe_2Se_3$ and $K_xFe_{2-y}Se_2$.[23,24] Using obtained Fe-Se and

TABLE II. Atomic coordinates, equivalent isotropic displacement parameters, and selected bond lengths and angles for $BaFe_2Se_2O$ measured at room temperature.

Atom	Wyckoff	x	y	z	U_{eq} ($\times 10^{-5}$ nm^2)
Ba	2b	3/4	1/4	0.49047(4)	7.34(9)
Fe	4f	0.58580(5)	3/4	0.87890(7)	9.15(11)
O	2a	3/4	3/4	0.7372(6)	8.9(5)
Se	4f	0.45734(4)	1/4	0.75887(5)	7.39(10)
		Interatomic Distances (nm)			
Fe-Se	0.24706(6)	Fe-Se	0.25540(4)	Fe-O	0.18769(19)
Ba-Se	0.33541(3)	Ba-Se	0.34008(4)	Ba-O	0.2649(2)
Ba-Fe	0.37012(4)				
		Bond Angles (°)			
Se-Fe-Se	103.050(15)	Se-Fe-Se	108.03(2)	Se-Fe-O	130.38(10)
Se-Fe-O	105.48(5)	Fe-Se-Fe	76.950(15)	Fe-Se-Fe	108.03(2)
Fe-O-Fe	119.1(2)				

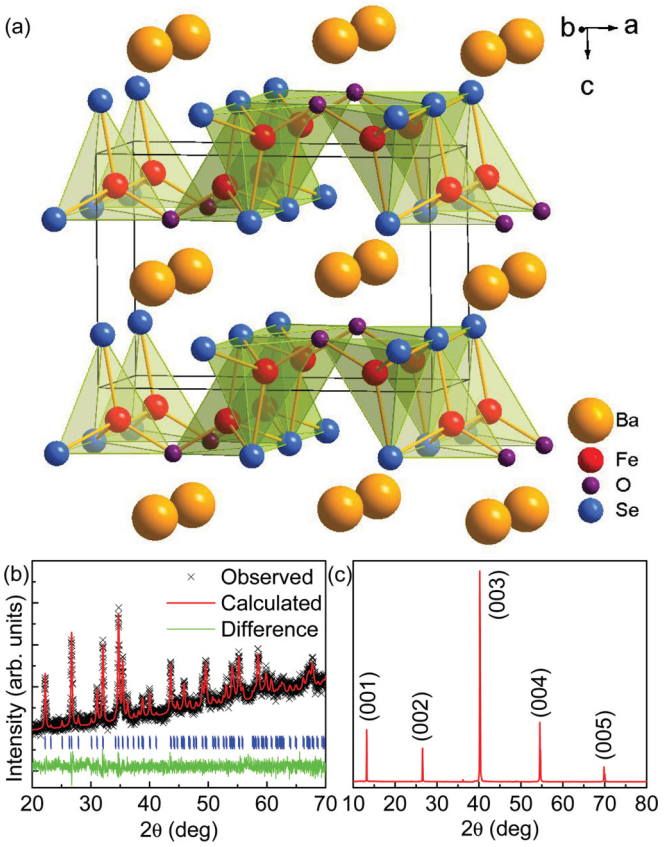

FIG. 1. (Color online) (a) Crystal structure of $BaFe_2Se_2O$. The biggest orange, big red, medium blue, and small purple balls represent Ba, Fe, O, and Se ions, respectively. (b) and (c) Powder and single-crystal XRD patterns of $BaFe_2OSe_2$.

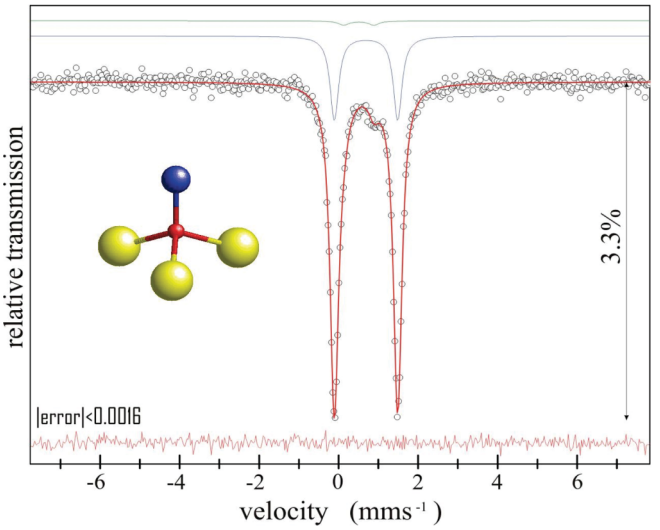

FIG. 2. (Color online) Mössbauer spectrum of $BaFe_2Se_2O$ at $T = 294$ K. Vertical arrow denotes relative position of peaks with respect to the background. The data were shown by open circles and the fit is given by the red solid line. The doublets of the main (bottom green line) and second phase (top green line; see text) are offset for clarity. Inset shows local coordination of Fe atoms in tetrahedra: The central smallest ball denotes Fe, the medium size ball shows oxygen, and the largest balls show selenium atoms.

Fe-O bond lengths as shown in Table II, the valence of Fe ions in $BaFe_2Se_2O$ can be calculated using the bond valence sum (BVS) formalism in which each bond with a distance d_{ij} contributes a valence $v_{ij} = \exp[(R_{ij} - d_{ij})/0.37]$ with R_{ij} as an empirical parameter and the total of valences of atom i, V_i, equals $V_i = \sum_j v_{ij}$.[25,26] The calculated valence of Fe ions is +2.23, slightly larger than the apparent oxidation state (+2) for Fe ions. Structural refinement of powder XRD results confirms that all reflections can be indexed in the *Pmmn* space group and the refined lattice parameters are $a = 0.9862(1)$ nm, $b = 0.4138(1)$ nm, and $c = 0.6732(1)$ nm, close to the values obtained from single-crystal XRD. Only (001) reflections were observed in the single-crystal XRD patterns of $BaFe_2Se_2O$ [Fig. 1(c)], indicating that the crystallographic c axis is perpendicular to the plane of the single crystal.

A Mössbauer fit of $BaFe_2Se_2O$ consists of two doublets corresponding to the paramagnetic state (Fig. 2). Based on the goodness of fit (0.9995), long-range magnetic order is unlikely at 294 K. The first doublet dominates the signal and takes 92% of the fit area with an isomer shift of 0.690(1) mm/s. The first coordination sphere of Fe (inset of Fig. 2) is tetrahedral with three selenium and one oxygen atoms. Fe^{2+} and Fe^{3+} in FeO_4 tetrahedra have isomer shift values (0.85–0.95) mm/s and (0.2–0.3) mm/s, respectively. The isomer shift drops with the increase of effective charge near ^{57}Fe. A smaller value of isomer shift in $BaFe_2Se_2O$ when compared to FeO_4 tetrahedra is consistent with larger covalency of Fe-Se bonds. The isomer shift is in agreement with the calculated value for Fe valence by BVS formalism. The quadrupole shift of 1.594(2) mm/s points to large distortion of tetrahedra. The second doublet has an isomer shift of 0.51(1) mm/s and 0.76(3) quadrupole splitting. These parameters are similar to what was observed in other Fe-Se compounds (β-FeSe and $FeSe_2$), pointing either to the presence of impurities or to intrinsic properties of the Fe environment in $BaFe_2Se_2O$.[27,28] If we assume similar recoil-free factors, about 8% of the fit area not covered by the main doublet would correspond to an approximately similar volume of the impurity crystallographic phase fraction. Such large impurity fraction would have been detected in our x-ray experiments. Therefore, the second doublet most likely reflects the contribution of the $FeSe_4$ tetrahedra in the $BaFe_2Se_2O$ crystal structure where Fe is tetrahedrally coordinated only by Se atoms with no O bonds present. The random distribution of $FeSe_4$ tetrahedra implies the presence of ionic bond disorder since about 8% of Fe is tetrahedrally coordinated by $FeSe_4$ instead of $FeSe_3O$. This could suggest the possible presence of vacancies on the O site, excess Se, and $BaFe_2Se_{2+\delta}O_{1-\delta}$ stoichiometry.

The local environments of Fe and Se such as bond distances are also analyzed by fitting the EXAFS data as shown in Fig. 3. For the Fe site, the nearest neighbors are one oxygen atom [$d_{Fe-O} = 0.18769(19)$ nm] and three Se atoms [1 × Se(I) and 2 × Se(II)] with two different distances [$d_{Fe-Se(I)} = 0.24706(6)$ nm and $d_{Fe-Se(II)} = 0.25540(4)$ nm]. The next-nearest neighbors are three Fe atoms [1 × Fe(I) and 2 × Fe(II)] with two different distances ($d_{Fe-Fe(I)} \sim 0.313$ nm bridged by O and $d_{Fe-Fe(II)} \sim 0.324$ nm bridged by Se). On

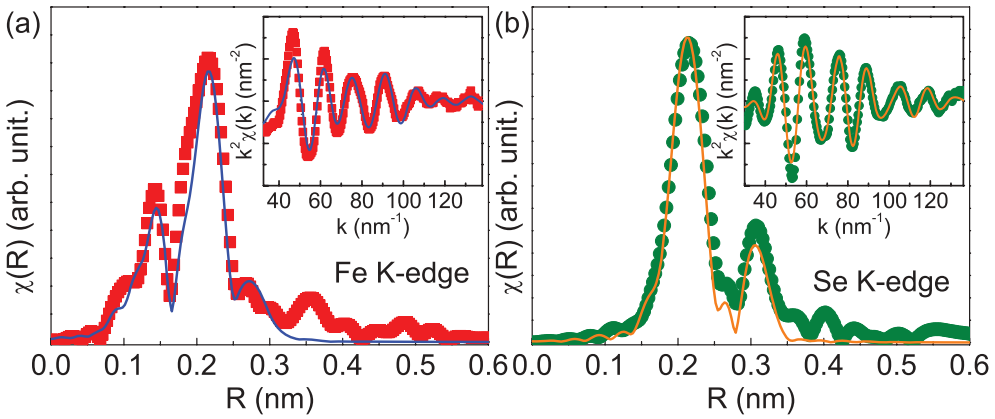

FIG. 3. (Color online) FT magnitudes of the EXAFS oscillations (symbols) for Fe k edge (a) and Se k edge (b). The model fits are shown as solid lines. The FTs are not corrected for the phase shifts and represent raw experimental data. Insets of (a) and (b): Filtered EXAFS (symbols) with k-space model fits (solid line).

the other hand, for the Se site, the nearest neighbors are three Fe atoms with bond distances $d_{\mathrm{Fe-Se(I)}}$ and $d_{\mathrm{Fe-Se(II)}}$. The next-nearest neighbors are three Ba atoms [$2 \times$ Ba(I) and $1 \times$ Ba(II)] with two different distances [$d_{\mathrm{Se-Ba(I)}} = 0.33541(3)$ nm and $d_{\mathrm{Se-Ba(II)}} = 0.34008(4)$ nm]. From the joint analysis of Fe and Se edge EXAFS data using a single-bond distance for Fe-O, Fe-Se, Fe-Fe, and Se-Ba, and by fitting the k range 20–140 nm^{-1} for the Fe K edge and 20–129 nm^{-1} for the Se K edge [insets of Figs. 3(a) and 3(b)], the fitted average bond lengths are $d_{\mathrm{Fe-O}} = 0.187(2)$ nm, $d_{\mathrm{Fe-Se}} = 0.2500(8)$ nm, $d_{\mathrm{Fe-Fe}} = 0.317(4)$ nm, and $d_{\mathrm{Se-Ba}} = 0.338(2)$ nm, which are consistent with the average bond distances derived from XRD fitting. It should be noted that the difference between experimental and theoretical spectra is due to the finite fitting range.

As shown in Fig. 4, the resistivity $\rho_{ab}(T)$ of the $BaFe_2Se_2O$ crystal increases rapidly with decreasing temperature, suggesting that this compound is an insulator in the measured temperature region. The high-temperature (above 240 K) data can be accurately described by the thermal activation

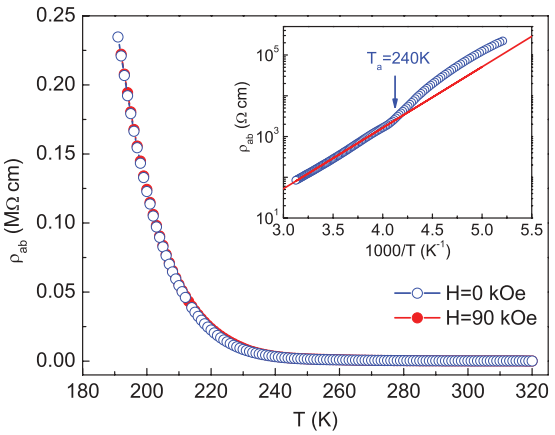

FIG. 4. (Color online) Temperature dependence of the resistivity $\rho_{ab}(T)$ of the $BaFe_2Se_2O$ crystal with $H = 0$ (closed blue square) and 90 kOe (open red circle; $H \| c$). Inset shows the fitting results of $\rho_{ab}(T)$ at zero field using thermal activation model. The red line is the fitted curve.

model $\rho_{ab}(T) = \rho_0 \exp(E_a/k_B T)$, where ρ_0 is a prefactor, $E_a = 296.7(8)$ meV is thermal activated energy, and k_B is the Boltzmann's constant. Moreover, the room-temperature resistivity $\rho_{ab}(300\ \mathrm{K})$ is about 163 Ω·cm. Overall, both E_a and $\rho_{ab}(T)$ are much larger than those in other known insulating iron selenides (see Table III), not to mention 5 mΩ·cm in metallic LaOFeAs. The metallic iron pnictides and chalcogenides are "Hund's metals,"[33,34] which are ready to be tuned to a Mott insulator upon increasing the Fe-Fe distance[32] or to a "Hund's insulator" with a selective shrinkage of the Fe-Fe bonds.[35] The much longer distance between nearest Fe-Fe neighbors ($d_{\mathrm{Fe-Fe}}$ in Table III) in $BaFe_2Se_2O$ would significantly reduce the electron bandwidth, rendering the material a Mott insulator.

It should be noted that there is an anomaly in resistivity at $T_a = 240$ K (inset in Fig. 4). As temperature decreases below T_a, $\rho_{ab}(T)$ increases faster than, and then bends to, what is expected from extrapolation of the high-temperature data (solid line). Thus, the low-temperature behavior of $\rho_{ab}(T)$ may be fitted to the expression of $\rho_0 \exp[(E_a/k_B T)^{\alpha}]$ where $\alpha < 1$, which means that the thermal activation of electron hopping is less effective. This indicates that below T_a the electrons are trapped by a new mechanism in addition to small polarons. Since the material is already an insulator above T_a, it is unlikely a density-wave transition. A similar anomaly accompanying antiferromagnetic transition has been observed in strongly correlated systems, such as $La_{0.67}Sr_{0.33}FeO_3$.[40] We thus attribute the transition at T_a to a long-range antiferromagnetic ordering in the Mott insulator (which will be studied below), which brings in the spin-polaron mechanism since electron hopping now distorts not only the lattice but also the spin order.[36–39]

The $\rho_{ab}(T)$ of $BaFe_2Se_2O$ is obviously different from the parent compounds of iron pnictide superconductors, such as LaFeAsO. LaFeAsO has much smaller absolute resistivity than $BaFe_2Se_2O$, and below the spin density wave (SDW) transition temperature, its resistivity drops significantly when compared to the faster increase of resistivity in $BaFe_2Se_2O$ below T_a.[41] The differences could be related to the different correlation strengths in these two systems. $BaFe_2Se_2O$ is in the Mott-insulating state. In iron-based superconductors

TABLE III. Comparing several known insulating iron selenides with nominal Fe^{2+}. d_{Fe-Fe} is the Fe-Fe bond length, E_a the thermal activation energy, ρ_{ab} the ab-plane room-temperature resistivity, and T_N the transition temperature to an antiferromagnetic long-range order.

Materials	$(Tl,K)Fe_{1.5}Se_2$	$BaFe_2Se_3$	$La_2O_2Fe_2OSe_2$	$BaFe_2Se_2O$
Reference	Ref. 29	Ref. 30 (Ref. 31)	Ref. 32	this manuscript
Coordination	$FeSe_4$ tetrahedron	$FeSe_4$ tetrahedron	$FeSe_6O_2$ octahedron	$FeSe_3O$ tetrahedron
Fe lattice	square lattice	ladder	square lattice	coupled ladders
d_{Fe-Fe} (nm)	0.276	0.272 (0.262, 0.283)	0.288	0.313
E_a (meV)	36	178	190	297
ρ_{ab} (300 K) (Ω·cm)	0.03	17	150	163
T_N (K)	250	256	90	240

the correlation strength is material and orbital dependent;[33] however most of ternary iron arsenide compounds are at the boundary of itinerancy and Mott localization and have intermediately strong electron correlations. The $\rho_{ab}(T)$ measured at $H = 90$ kOe indicates that there is no obvious magnetoresistance (MR) in $BaFe_2Se_2O$ [MR $= \rho_{ab}(90\,\text{kOe}) - \rho_{ab}(0)/\rho_{ab}(90\,\text{kOe}) < 4\%$] (Fig. 4), which is similar to $BaFe_2Se_3$,[30] and in contrast to LaFeAsO.[41]

The magnetic susceptibility $\chi(T)$ of the $BaFe_2OSe_2$ single crystal is plotted in Fig. 5(a). There is a peak in the $d(\chi T)/dT$ curve[42] at $T_1 = 240$ K, for $H \parallel ab$, and the values of susceptibility between ZFC and FC curves are nearly the same at this temperature. This peak corresponds to the AFM transition temperature $T_N = 240$ K, which coincides with T_a of the resistivity anomaly and is confirmed by specific-heat

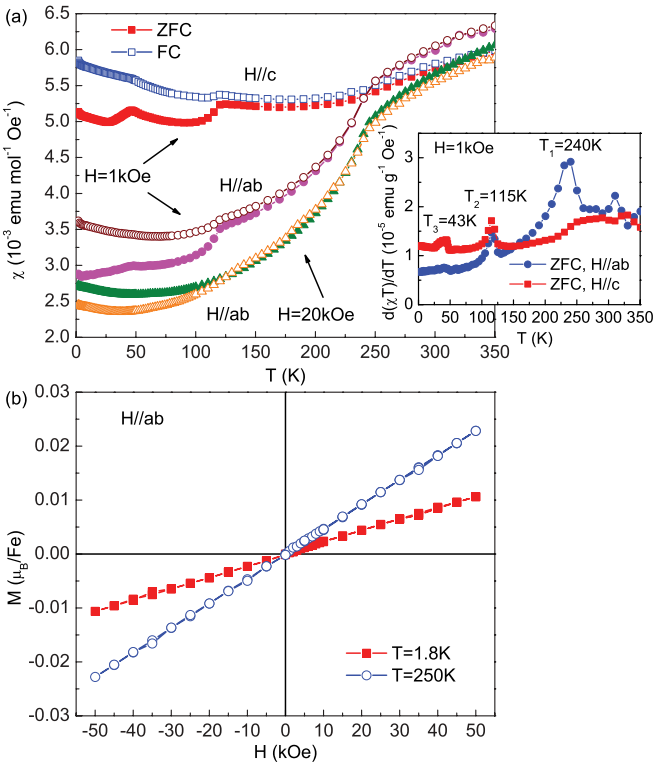

FIG. 5. (Color online) (a) Temperature dependence of dc magnetic susceptibility $\chi(T)$ under ZFC and FC modes along ab plane and c axis with different fields. (b) Isothermal magnetization hysteresis loops $M(H)$ for $H \| ab$ at $T = 1.8$ K and 250 K.

measurements shown below. The Mössbauer fit indicates that long-range magnetic order is absent at 294 K. Moreover, the decrease in $\chi_{ab}(T)$ with temperature is more significant than $\chi_c(T)$. This suggests that the easy axis of the magnetization direction could be in the ab plane. According to mean-field theory for collinear antiferromagnets, $\chi(T) \to 0$ along the easy-axis direction whereas it is nearly constant below T_N for the field perpendicular to the easy-axis direction. Above T_N, the Curie-Weiss temperature dependence is not observed up to 350 K. Instead, $\chi(T)$ increases with T in the measured region. This is reminiscent of the linear increase of $\chi(T)$ above T_N in a variety of materials with $[TM_2OCh_2]^{2-}$, which was attributed to the presence of frustrated magnetic interactions.[8,9,11]

With further decreasing temperature below T_N, there are two additional peaks in the $d(\chi T)/dT$ curve at $T_2 = 115$ K and $T_3 = 43$ K, respectively [inset of Fig. 5(a)]. In particular, $\chi(T)$ drops abruptly at 115 K with much less anisotropy, suggesting that a new gap opens for magnetic excitations. For $\chi(T)$ at $H = 20$ kOe, those transitions are almost suppressed and the shape of the curve is very similar to the results reported by Han *et al.*[43] A possible scenario for these unusual magnetic behaviors is the formation of spin singlet dimers.[44–46] This can be facilitated by the interesting structure of $BaFe_2OSe_2$: The oxygen bridged Fe-Fe distance is considerably shorter and thus likely produces much stronger antiferromagnetic superexchange interaction between neighboring Fe spins than the other Fe-Fe paths (bridged by Se). Since $\chi(T)$ remains finite for all T, those spin dimers are likely droplets in the matrix of antiferromagnetically ordered spins, or there is a phase separation. From the drop of $\chi(T)$ at 115 K, the relative volume of the supposed dimers is roughly estimated to be about 10%. The spin frustration from the competition between the antiferromagnetic long-range order and the spin dimerization may account for the absence of Curie-Weiss law above T_N.

The absence of hysteresis in isothermal $M(H)$ loops for $H \| ab$ [Fig. 5(b)] at $T = 1.8$ K and 250 K indicates that there are no ferromagnetic impurities. Moreover, the slope of $M(H)$ increases with increasing temperature consistent with the AFM behavior observed in $\chi(T)$ curves [Fig. 5(b)].

As shown in Fig. 6, the specific heat C_p of $BaFe_2Se_2O$ is close to the value of $3NR$ at high temperature ($T = 300$ K) assuming $N = 6$, where N is the number of atoms in the chemical formula and R is the gas constant ($R = 8.314\,\text{J mol}^{-1}\,\text{K}^{-1}$). It confirms the number of atoms for $BaFe_2Se_2O$ obtained from single-crystal XRD fitting. At low temperature, the $C_p(T)$ curve can be fitted by a cubic term βT^3 (inset of Fig. 6) and

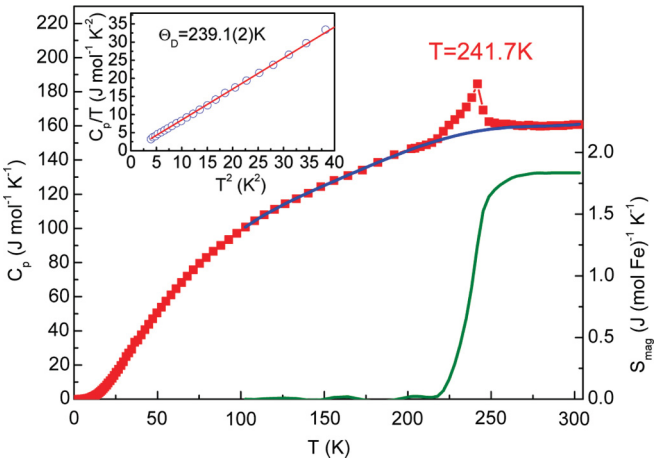

FIG. 6. (Color online) Temperature dependence of specific heat for $BaFe_2Se_2O$ crystal. The blue curve represents the phonon contribution fitted by a polynomial. The right axis and its associated green solid curve denote the magnetic entropy. Inset: The low-temperature specific-heat data in the plot of C_p/T vs T^2. The red solid line is the fitting curve using formula $C_p/T = \beta T^2$.

the fitted value β is 0.852(2) mJ mol^{-1} K^{-4}. According to the formula $\Theta_D = (12\pi^4 NR/5\beta)^{1/3}$, the Debye temperature is estimated to be $\Theta_D = 239.1(2)$ K. The larger Θ_D when compared to $BaFe_2Se_3$ [$\Theta_D = 205(1)$ K] can be ascribed to the smaller atomic mass of oxygen than selenium.[23]

There is a λ-type anomaly at $T_1 = 241.7$ K as shown in Fig. 6. The peak position is very close to the peak position ($T_1 = 240$ K) at the $d\chi(T)/dT$ curve [inset of Fig. 5(a)]. This suggests that a long-range AFM ordering forms at this temperature. After subtraction the phonon contribution ($C_{\rm ph}$) fitted using a polynomial for the total specific heat, the magnetic contribution ($C_{\rm mag}$) can be obtained. The magnetic entropy can be calculated using the integral $S_{\rm mag}(T) = \int_0^T C_{\rm mag}/T\,dT$. The derived $S_{\rm mag}$ is ~1.83 J/mol-K when T is up to 300 K (Fig. 6), which is much smaller than expected values $R\ln(2S+1)$ for Fe^{2+} ions with low spin state (~20% $R\ln 3$) and with high spin state (~13.7% $R\ln 5$) in tetrahedral crystal fields. It is even less than $R\ln 2$ for $S = 1/2$ (~31.8% $R\ln 2$), suggesting that there is short-range magnetic order at higher temperature which partially releases the magnetic entropy before any long-range magnetic transition.

Although undoped iron pnictide compounds also exhibit small heat capacity peak, i.e., small magnetic entropy $S_{\rm mag}$ releasing at $T_{\rm SDW}$, this should be due to a different origin when compared to $BaFe_2Se_2O$. The small value of $S_{\rm mag}$ in parent materials of iron pnictide superconductors can be ascribed to the itinerancy of Fe ions.[47] $BaFe_2Se_2O$ is an insulator; hence the small value of $S_{\rm mag}$ could not be due to the itinerancy of the Fe moment but is due to the short-range AFM order above T_N (240 K), consistent with Mössbauer spectrum and magnetization measurement results. It is also confirmed by Ref. 43. Similar small $S_{\rm mag}$ has been observed in other compounds containing $[TM_2OSe_2]^{2-}$ layers due to the existence of short-range AFM order above the long-range AFM ordering temperature T_N.[9,12] On the other hand, there is no noticeable change in C_p at $T_2 = 115$ K and $T_3 = 43$ K, indicating that the possible spin dimers coexisting with the antiferromagnetic long-range order do not fluctuate among different oxygen-bridged Fe-Fe bonds and are locked in real space. This can be verified by investigating whether the oxygen-bridged Fe-Fe distance is changed abruptly at those temperatures. Detailed low-temperature magnetic and structural properties of $BaFe_2Se_2O$ and comparison with iron arsenide compounds[41,48–51] will be addressed in a forthcoming work.

IV. CONCLUSION

In summary, we report on a layered iron oxychalcogenide, $BaFe_2Se_2O$. The crystal structure features double chains of edge-shared Fe-Se(O) tetrahedra that propagate along the b axis. The Fe-Se(O) double chains are bridged by oxygen along the a axis. $BaFe_2Se_2O$ single crystals are magnetic semiconductors with a long-range anisotropic AFM transition at 240 K and two transitions at 115 K and 43 K where magnetic susceptibility drops abruptly. The magnetic entropy up to 300 K is much smaller than expected for Fe^{2+} in tetrahedral crystal fields, suggesting the existence of short-range AFM correlation above room temperature. This material turns out to be a magnetic insulator at the borderline between the long-range antiferromagnetic spin order and likely spin dimers. Because of the interesting structure and connectivity among the iron atoms, it is of interest to investigate the mechanism of the magnetic ground state by theoretical calculations and by neutron scattering experiments. Moreover, doping effects on physical properties should further reveal similarities and differences with superconducting iron selenide compounds.

Note added. Recently, we became aware that Han *et al.*[43] also synthesized $BaFe_2Se_2O$. They concluded that this material is a Mott insulator with a magnetic transition to the Néel state around 240 K. $BaFe_2Se_2O$ crystals in our work have somewhat higher resistivity at room temperature and much higher resistivity at low temperatures which could be caused by different oxygen stoichiometry and/or site occupancy. Note that there is a clear discontinuity in resistivity at magnetic transition in our crystals, as opposed to crystals in Ref. 43, suggesting that indeed a different fitting model of $\rho(T)$ below magnetic transition is justified. In addition, magnetic entropy release in heat capacity at the magnetic ordering temperature is smaller for our crystals when compared to crystals in Ref. 43. This suggests a higher contribution of short-range magnetic order probably induced by stoichiometry deviation.

ACKNOWLEDGMENTS

We thank Alexei M. Tsvelik and Kefeng Wang for helpful discussion, and Syed Khalid for help with XAFS measurements. Work at Brookhaven is supported by the US DOE under Contract No. DE-AC02-98CH10886. A.I.F. acknowledges support by US Department of Energy Grant No. DE-FG02-03ER15476. Beamline X19A at the NSLS is supported in part by US Department of Energy Grant No. DE-FG02-05ER15688. This work has also been supported by Grant No. 171001 from the Serbian Ministry of Education and Science.

[1] Y. Kamihara, T. Watanabe, M. Hirano, and H. Hosono, J. Am. Chem. Soc. **130**, 3296 (2008).

[2] S. J. Clarke, P. Adamson, S. J. C. Herkelrath, O. J. Rutt, D. R. Parker, M. J. Pitcher, and C. F. Smura, Inorg. Chem. **47**, 8473 (2008).

[3] S. Adachi, T. Tatsuki, T. Tamura, and K. Tanabe, Chem. Mater. **10**, 2860 (1998).

[4] K. Ueda, S. Inoue, S. Hirose, H. Kawazoe, and H. Hosono, Appl. Phys. Lett. **77**, 2701 (2000).

[5] H. Hiramatsu, K. Ueda, H. Ohta, M. Hirano, T. Kamiya, and H. Hosono, Appl. Phys. Lett. **82**, 1048 (2003).

[6] H. Kamioka, H. Hiramatsu, H. Ohta, M. Hirano, K. Ueda, T. Kamiya, and H. Hosono, Appl. Phys. Lett. **84**, 879 (2004).

[7] J. M. Mayer, L. F. Schneemeyer, T. Siegrist, J. V. Waszczak, and B. v. Dover, Angew. Chem., Int. Ed. Engl. **31**, 1645 (1992).

[8] C. Wang, M.-Q. Tan, C.-M. Feng, Z.-F. Ma, S. Jiang, Z.-A. Xu, G.-H. Cao, K. Matsubayashi, and Y. Uwatoko, J. Am. Chem. Soc. **132**, 7069 (2010).

[9] N. Ni, E. Climent-Pascual, S. Jia, Q. Huang, and R. J. Cava, Phys. Rev. B **82**, 214419 (2010).

[10] F. Han, X. Y. Zhu, G. Mu, P. Cheng, and H.-H. Wen, Phys. Rev. B **78**, 180503 (2008).

[11] H. Kabbour, E. Janod, B. Corraze, M. Danot, C. Lee, M.-H. Whangbo, and L. Cario, J. Am. Chem. Soc. **130**, 8261 (2008).

[12] R. H. Liu, J. S. Zhang, P. Cheng, X. G. Luo, J. J. Ying, Y. J. Yan, M. Zhang, A. F. Wang, Z. J. Xiang, G. J. Ye, and X. H. Chen, Phys. Rev. B **83**, 174450 (2011).

[13] H. C. Lei, E. S. Bozin, A. Llobet, V. Ivanovski, V. Koteski, J. Belosevic-Cavor, B. Cekic, and C. Petrovic, Phys. Rev. B **86**, 125122 (2012).

[14] X. C. Wang, Q. Q. Liu, Y. X. Lv, W. B. Gao, L. X. Yang, R. C. Yu, F. Y. Li, and C. Q. Jin, Solid State Commun. **148**, 538 (2008).

[15] D. R. Parker, M. J. Pitcher, P. J. Baker, I. Franke, T. Lancaster, S. J. Blundell, and S. J. Clarke, Chem. Commun. **16**, 2189 (2009).

[16] J. B. He, D. M. Wang, H. L. Shi, H. X. Yang, J. Q. Li, and G. F. Chen, Phys. Rev. B **84**, 205212 (2011).

[17] APEX2 Ver. 2008.5; Bruker AXS, Inc., Madison, WI (2008).

[18] G. M. Sheldrick, Acta Crystallogr. A **64**, 112 (2008).

[19] B. Hunter, RIETICA, A Visual Rietveld Program, International Union of Crystallography Commission on Powder Diffraction Newsletter No. 20 (Summer 1998); http://www.rietica.org.

[20] R. Prins and D. Koningsberger, *X-Ray Absorption: Principles, Applications, Techniques of EXAFS, SEXAFS, XANES* (Wiley, New York, 1988).

[21] R. A. Brand, WinNormos Mössbauer fitting program, Universität Duisburg, 2008.

[22] J. Guo, S. Jin, G. Wang, S. Wang, K. Zhu, T. Zhou, M. He, and X. Chen, Phys. Rev. B **82**, 180520(R) (2010).

[23] H. C. Lei, H. J. Ryu, A. I. Frenkel, and C. Petrovic, Phys. Rev. B **84**, 214511 (2011).

[24] H. C. Lei, M. Abeykoon, E. S. Bozin, K. F. Wang, J. B. Warren, and C. Petrovic, Phys. Rev. Lett. **107**, 137002 (2011).

[25] I. D. Brown and D. Altermatt, Acta Crystallogr. Sect. B **41**, 244 (1985).

[26] N. E. Brese and M. O'Keeffe, Acta Crystallogr. Sect. B **47**, 192 (1991).

[27] C. E. M. Campos, V. Drago, J. C. de Lima, T. A. Grandi, K. D. Machado, and M. R. Silva, J. Magn. Magn. Mater. **269**, 6 (2004).

[28] A. Blachowski, K. Ruebenbauer, J. Zukrowski, J. Przewoznik, K. Wojciechowski, and Z. M. Stadnik, J. Alloy Compnd. **494**, 1 (2010).

[29] M.-H. Fang, H.-D. Wang, C.-H. Dong, Z.-J. Li, C.-M. Feng, J. Chen, and H. Q. Yuan, Europhys. Lett. **94**, 27009 (2011).

[30] H. C. Lei, H. J. Ryu, A. I. Frenkel, and C. Petrovic, Phys. Rev. B **84**, 214511 (2011).

[31] J. M. Caron, J. R. Neilson, D. C. Miller, A. Llobet, and T. M. McQueen, Phys. Rev. B **84**, 180409(R) (2011).

[32] J.-X. Zhu, R. Yu, H. D. Wang, L. L. Zhao, M. D. Jones, J. H. Dai, E. Abrahams, E. Morosan, M. H. Fang, and Q. M. Si, Phys. Rev. Lett. **104**, 216405 (2010).

[33] Z. P. Yin, K. Haule, and G. Kotliar, Nat. Mater. **10**, 932 (2011).

[34] W.-G. Yin, C.-C. Lee, and W. Ku, Phys. Rev. Lett. **105**, 107004 (2010).

[35] W.-G. Yin, C.-H. Lin, and W. Ku, Phys. Rev. B **86**, 081106(R) (2012).

[36] S. Schmitt-Rink, C. M. Varma, and A. E. Ruckenstein, Phys. Rev. Lett. **60**, 2793 (1988).

[37] G. Martinez and P. Horsch, Phys. Rev. B **44**, 317 (1991).

[38] Z. Liu and E. Manousakis, Phys. Rev. B **45**, 2425 (1992).

[39] W.-G. Yin, C.-D. Gong, and P. W. Leung, Phys. Rev. Lett. **81**, 2534 (1998).

[40] M. Imada, A. Fujimori, and Y. Tokura, Rev. Mod. Phys. **70**, 1039 (1998).

[41] M. A. McGuire, A. D. Christianson, A. S. Sefat, B. C. Sales, M. D. Lumsden, R. Jin, E. A. Payzant, D. Mandrus, Y. Luan, Veerle Keppens, V. Varadarajan, J. W. Brill, R. P. Hermann, M. T. Sougrati, F. Grandjean, and G. J. Long, Phys. Rev. B **78**, 094517 (2008).

[42] M. E. Fisher, Philos. Mag. **7**, 1731 (1962).

[43] F. Han, X. Wan, B. Shen, and H.-H. Wen, Phys. Rev. B **86**, 014411 (2012).

[44] T. Giamarchi, C. Rüegg, and O. Tchernyshyov, Nat. Phys. **4**, 198 (2008).

[45] T. Giamarchi and A. M. Tsvelik, Phys. Rev. B **59**, 11398 (1999).

[46] T. Nikuni, M. Oshikawa, A. Oosawa, and H. Tanaka, Phys. Rev. Lett. **84**, 5868 (2000).

[47] C. Krellner, N. Caroca-Canales, A. Jesche, H. Rosner, A. Ormeci, and C. Geibel, Phys. Rev. B **78**, 100504(R) (2008).

[48] M. Tegel, S. Johansson, V. Weiß, I. Schellenberg, W. Hermes, R. Pöttgen, and D. Johrendt, Europhys. Lett. **84**, 67007 (2008).

[49] S. Kitao, Y. Kobayashi, S. Higashitaniguchi, M. Saito, Y. Kamihara, M. Hirano, T. Mitsui, H. Hosono, and M. Seto, J. Phys. Soc. Jpn. **77**, 103706 (2008).

[50] Z. Li, Y. Fang, X. Ma, H. Pang, and F. Li, Phys. Rev. B **84**, 134509 (2011).

[51] H.-H. Klauss, H. Luetkens, R. Klingeler, C. Hess, F. J. Litterst, M. Kraken, M. M. Korshunov, I. Eremin, S.-L. Drechsler, R. Khasanov, A. Amato, J. Hamann-Borrero, N. Leps, A. Kondrat, G. Behr, J. Werner, and B. Büchner, Phys. Rev. Lett. **101**, 077005 (2008).